

Rajesh Sadanandan, Peter Kutne, Adam Steinberg, Wolfgang Meier
Investigation of the syngas flame characteristics at elevated pressures using
optical and laser diagnostic methods
Flow, Turbulence and Combustion 89, (2012) 275-294.

The original publication is available at www.springerlink.com

<http://dx.doi.org/10.1007/s10494-011-9354-z>

Investigation of the Syngas Flame Characteristics at Elevated Pressures Using Optical and Laser Diagnostic Methods

Rajesh Sadanandan · Peter Kutne · Adam
Steinberg · Wolfgang Meier

Received: date / Accepted: date

Abstract The effect of pressure on the characteristics of syngas flames is investigated under gas turbine relevant conditions using planar laser induced fluorescence of OH radicals and OH* chemiluminescence imaging. An optically accessible combustor fitted with a swirl burner was operated with two different syngas mixtures, preheated air at 700 K, and pressures ranging from 5 to 20 bars. The thermal load varied from 15 to 25 kW/bar at an equivalence ratios 0.5. The OH-PLIF measurements show that the flames under all conditions exhibited two reaction fronts, one at the shear layer between the inner recirculation zone

R. Sadanandan

Institut für Verbrennungstechnik, DLR Stuttgart, Pfaffenwaldring 38-40, 70569 Stuttgart, Germany

E-mail: Rajesh.Sadanandan@dlr.de

P. Kutne

E-mail: Peter.Kutne@dlr.de ·

A. Steinberg

E-mail: Adam.Steinberg@dlr.de ·

W. Meier

E-mail: Wolfgang.Meier@dlr.de

and the fuel inlet, and one between the fuel inlet and the air nozzle. The more or less continuous reaction front at low pressure turned into a highly corrugated flame front at higher pressures, with isolated regions of ignition and extinction. The probability density distribution of the flame curvature for the mixtures studied showed that the inner and outer flame responded differently to the pressure increase, with the mean curvature magnitude also depending on the mixture composition and thermal load. The measurements clearly show the limitations associated with the use of OH^* chemiluminescence images as a marker for the heat release rate especially in case of syngas mixtures.

Keywords Syngas fuels · gas turbine combustion · Laser Induced Fluorescence · chemiluminescence · flame curvatures

1 Introduction

Coal is one of the most polluting energy sources with respect to nitrogen oxides, sulphur oxides, and particulate matter emissions. It is also the most carbon intensive energy source. It is therefore imperative for us to develop more energy efficient coal technology to minimise the harmful pollutant emissions. One of the emerging clean coal technologies is the integrated gasification combined cycle (IGCC). The process involves reformation of carbon rich fossil fuel like coal in a pre-combustion phase via coal gasification to produce hydrogen-rich synthesis gas (syngas) and a high concentration of CO_2 . The high CO_2 concentration helps in improving the operational efficiency of CO_2 post combustion separation units using an amine-process [1]. The syngas mixture can be used to power conventional gas- and/or steam-turbine power plants. One critical problem with syngas combustion is the lack of available data that describe the combustion properties of such mixtures. The diverse composition of syngas, which consist of CO , H_2 , CH_4 , CO_2 , H_2O and various trace in dif-

ferent concentration, leads to significant variations in combustion properties. The specific composition depends on the fuel source and the processing techniques. Information about fundamental properties like flame speed, reactivity, and ignition delay times is vital as these influence the key combustion characteristics such as flame spatial distribution, flash back, and blowoff. The ability to predict combustion properties like flammability range, flame propagation speed, and combustion products of engines running on syngas fuels will thus be difficult without adequate information in the form of experimental and numerical databases.

For technical combustors like those in gas turbines, reliable experimental data and validated models at high pressures are mandatory. While there is a considerable amount of data available on syngas mixtures at atmospheric and low pressures [2–5], data available on technically relevant high pressure conditions are sparse. Under laminar boundary conditions, both GRI [6] and H_2/CO mechanism from Davis et al. [7] reproduced the experimental results reasonably well. Laminar flame speed, which is one of the fundamental properties characterizing a combustible mixture at a given temperature, pressure, and composition, of syngas mixtures has been measured [8] and modeled up to 40 atmospheres by Sun et al [9]. Natarajan et al. reported the influence of preheat temperature [10] and CO_2 dilution [11] on H_2/CO mixtures at elevated pressures both experimentally and numerically. Sung et al. conducted experimental and numerical investigation on the ignition and flame propagation characteristics of H_2/CO mixtures at elevated pressures to identify the controlling reactions in the H_2/CO kinetics [12].

However, there are not many research works, either experimental or computational, performed to understand the behaviour of turbulent syngas flames operating in lean regimes and high pressures such as in gas turbines. The current study, conducted at the German Aerospace Center (DLR) in Stuttgart, investigates the effects of pressure on flame characteristics under gas turbine relevant conditions. The long term goal is to develop numerical simu-

lation codes to predict the combustion properties of syngas fuels under such conditions. The project is part of the research project VESKO ("Verbrennung von Synthesegas aus Kohle in Gasturbinen") funded by the German Federal Ministry of Economics and Technology. The diagnostic methods employed in this study include planar laser-induced fluorescence of the hydroxyl radical (OH-PLIF) and chemiluminescence imaging of the electronically excited OH radical (OH^{*}). The OH^{*} images provided information about the size and shape of the heat release zones, whereas the OH-PLIF images were used to identify the reaction zones and the regions of burned gas [13, 14]. The experimental data generated are used for validation and optimisation of numerical simulation codes [15], and are a continuation of similar investigations conducted at atmospheric conditions [16].

2 Experimental Facility

2.1 Burner Geometry and High Pressure Test Facility

The gaseous fuelled swirl-flame burner (Fig. 1) used for the current research was developed at the University of Twente [17] and is described in detail elsewhere [16, 18]. It consists of a dual-annular nozzle with a circular bluff body of diameter 10 mm located along its central axis. The fuel nozzle ($\varnothing = 14$ mm) surrounds the bluff body and is surrounded in turn by the annular air nozzle (i.d. = 16 mm, o.d. = 30 mm). Both the fuel and air flows are swirled by radial swirlers. The flames were confined by a combustion chamber with a cross section of 85 X 85 mm and a height of 120 mm. Four quartz plates held by posts in the corners enabled almost unrestricted optical access to the flame. For the pressurized experiments (p up to 20 bar), the posts, front plate, and exhaust section were water cooled. The gases for the fuel mixtures (H₂, CH₄, CO, and N₂) were metered individually and mixed in-line before being supplied to the burner.

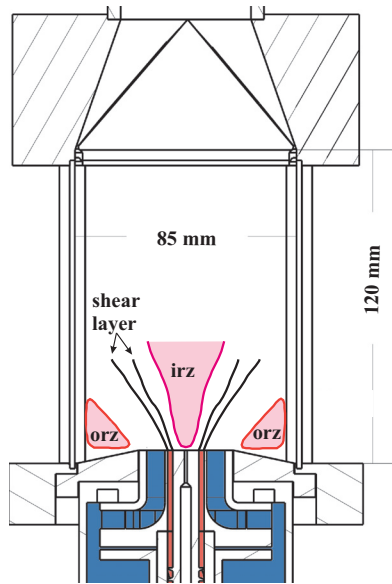


Fig. 1 Schematic of the burner with air inlet (blue), fuel inlet (red) and combustion chamber. The inner tube was not used in this experiment. The inner and outer recirculation zones of the flow field are indicated by irz and orz respectively.

The burner was installed in an optically accessible high pressure test facility (HBK-S) at the Institute of Combustion Technology in Stuttgart. Thermocouples and probes at different locations of the test rig were used to measure the temperature and pressure (absolute and differential) respectively, at different locations of the test rig during the tests. The main air, supplied from a compressor, was electrically preheated to the required experimental conditions before entering the combustion chamber. The air flows into the pressure vessel from downstream of the combustor and passes the outer surface of the combustion chamber in order to cool the windows before it is supplied to the burner. Orifice flow meters and high precision Coriolis flow meters were used to regulate the main air and fuel flow rates respectively.

2.2 Operating Conditions

In the current paper, flames with two different mixtures are investigated. The main fuel components were H_2 and N_2 , and the minor components were CO and CH_4 . The mixture compositions of the investigated gases are shown in Table. 1

Table 1 Fuel gas composition in volume fractions.

Fuel type	CH_4	H_2	CO	N_2	kJ/m^3
E5	0.00	42.54	2.37	55.09	4874
E6	3.66	45.63	0.44	50.27	6295

These represent the hydrogen rich syngases that are produced after the gasification of lignite or coal, followed by a CO shift reaction and sequestration of CO_2 . The high N_2 content in the mixture stems from the blending of nitrogen in the gasification air with the fuel gas.

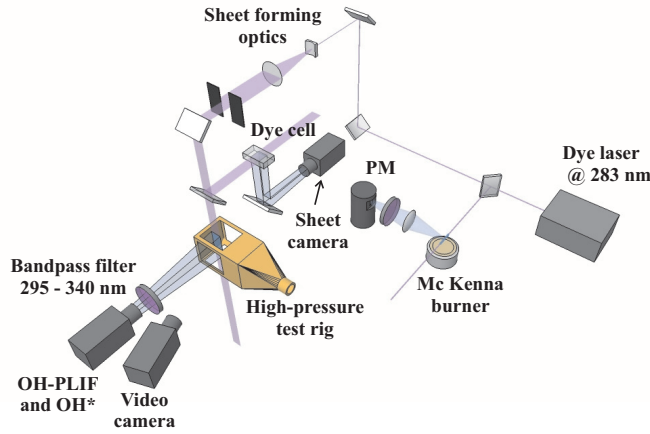
The flow conditions (pressure, flow velocities, flow rates) corresponding to the different flames reported in this paper are listed in Table. 2. Experiments were performed at an equivalence ratio $\phi = 0.5$ and the total thermal power varied between 75 kW and 500 kW. The inlet temperature of the fuel and air were 295 K and 700 K respectively. Further information about the velocity field inside the combustor can be found in [16, 18].

2.3 Experimental Set-up and Diagnostic Methods

Figure 2 shows the schematic of the diagnostic set-up used for the measurements. The diagnostic methods employed are OH^* (electronically excited) chemiluminescence imaging and Planar Laser Induced Fluorescence of the hydroxyl radical (OH-PLIF). OH^* images are

Table 2 Flame parameters.

Fuel type	P_{th} (kW/bar)	p (bar)	v_{fuel} (m/s)	v_{air} (m/s)	m_{CH_4} (g/s)	m_{H_2} (g/s)	m_{CO} (g/s)	m_{N_2} (g/s)	m_{air} (g/s)
E5	15	5	44.9	33.5	0.0	0.59	0.43	10.6	42.66
E5	15	10	44.9	33.5	0.0	1.18	0.85	21.20	85.32
E5	15	15	44.9	33.5	0.0	1.77	1.28	31.8	127.98
E5	15	20	44.9	33.5	0.0	2.36	1.71	42.4	170.64
E6	15	5	34.7	35.1	0.31	0.49	0.06	7.49	44.65
E6	15	10	34.7	35.1	0.63	0.98	0.12	14.98	89.29
E6	15	15	34.7	35.1	0.94	1.47	0.18	22.47	133.94
E6	15	20	34.7	35.1	1.25	1.96	0.25	29.96	178.59
E5	25	5	74.8	55.8	0.0	0.98	0.71	17.67	71.10
E5	25	10	74.8	55.8	0.0	1.96	1.42	35.33	142.2
E5	25	15	74.8	55.8	0.0	2.95	2.13	53.00	213.30

**Fig. 2** Schematic of the diagnostic set-up used for the high pressure measurements; PM - Photo Multiplier.

used to identify the size, shape, and location of the heat release zone, whereas OH-PLIF measurements were used to identify the high temperature zones and flame fronts.

A laser system, consisting of a flashlamp pumped, frequency doubled Nd:YAG laser (Quanta Ray, DCR-2) pumping a frequency doubled tuneable dye laser (Lumonics, HD-500)

at 10 Hz was used for the OH-PLIF measurements. The output of the dye laser was tuned to the $Q_1(8)$ transition of the OH A-X (1,0) system at approximately 283 nm. The output beam had a pulse energy of approximately 5 mJ. Part of this beam was sent to a stoichiometric CH_4/air reference flame stabilized on a McKenna burner. The OH-LIF produced by this flame was used for online monitoring of the OH excitation wavelength. Cylindrical lenses were used to expand the main laser beam into a sheet of 55 mm height and approximately 400 μm thickness at the beam waist inside the combustor.

On the detection side, an ICCD camera (Roper Scientific, 512 x 512 pixels) was used for capturing both OH* chemiluminescence and OH-PLIF signals at 90 degrees to the flow direction. The camera was equipped with an achromatic UV lens (Halle, $f/2$, $f = 64$ mm) and a UV interference filter (peak transmission at $\approx 315 \pm 15$ nm bandwidth). The camera exposure time was set to 400 ns and 40 μs for the OH-PLIF and OH* chemiluminescence measurements respectively. A beam splitter was used to deflect a small portion of the laser sheet into a rectangular quartz cell filled with fluorescent solution. The quartz cell, with a cross section of 10 x 10 mm² and 100 mm in height, is filled with a solution of Rhodamin dye in methanol. The fluorescence produced in the cell was captured simultaneously with the OH-PLIF instantaneous images using a second ICCD camera (Roper Scientific, 512 x 512 pixels) equipped with a Nikon objective ($f/4.0$, $f = 50$ mm). This image was used to correct the shot-to-shot laser sheet profile inhomogeneities. Both OH-PLIF and OH* images were corrected for background noise and for dark signal (fixed pattern signal that occurs with no light incident on the detector). The time synchronisation between the laser and the cameras was achieved by means of a pulse delay generator (SRS inc., type DG535)

Chemiluminescence emissions produced from flame reactions were used to gather information about the flame zone. OH* is the most frequently used indicator species and was employed here. Since the signals were line of sight integrated, resolution of individual spa-

tial structures was not possible. The key OH^* producing reaction in syngas flames containing H_2 and CO is reported in the literature as [19]



For hydrocarbon flames, the main formation reaction is found to be [19]



For the mixtures studied in the current investigation, reaction (1) may play a major role for the E5 flames, whereas for the E6 flames, both reactions (1) and (2) could describe the key formation steps. Reaction (2) will be relevant in the reaction zone where CH is formed in the E6 flames, whereas reaction (1) will dominate the overall reaction in both E5 and E6 at all pressures. In addition, with increasing pressure, the characteristic time scales of the three-body reaction (1) decreases, thereby playing a crucial role at higher pressures.

3 Estimation of Flame Curvature Probability Density Function from OH-PLIF

Images

Quantitative evaluation of topographic properties of the flame surface requires reducing the measured OH PLIF signals to mathematical contours representing the geometry of the instantaneous reaction layers. However detectable levels of OH exist not only in the reaction layers, but also in the high-temperature products above approximately 1500 K [20]. OH PLIF measurements therefore detect broad regions of OH as shown in Fig. 3 and consideration of additional properties of the OH signal is needed to identify the flame topography. Sadanandan et al. [21] showed that the reaction layers in swirl flames can be visualized by regions of high OH gradient. That is, OH concentrations increase exponentially

with temperature and reach super-equilibrium concentrations in the reaction layers. The OH signal gradients associated with generation of super-equilibrium OH in the reaction layers were observed to be considerably higher than those associated with the relaxation of super-equilibrium OH to equilibrium away from the reaction layers [22, 23].

A first estimate for the reactive flame surface therefore was made by placing a global threshold on the OH gradient signal. This resulted in continuous bands, several pixels in thickness, which followed the flame topography. These bands were reduced to mathematical contours by identifying the edge of the high OH-gradient region that lay in the low OH-signal region. Each thin reaction layer then was treated as a parametrically defined contour, $f(\varphi) = x_f(\varphi)\hat{e}_x + y_f(\varphi)\hat{e}_y$, where \hat{e}_x and \hat{e}_y are the respective unit vectors in the radial and axial directions. Results reported here describe the curvature of these contours, which was calculated as:

$$C = \frac{x'_f y''_f - y'_f x''_f}{(x'^2_f + y'^2_f)^{3/2}} \quad (3)$$

where $(\cdot)'$ and $(\cdot)''$ represent derivatives with respect to φ .

The resolution of the derived flame topography contours was the same as that of the OH PLIF measurements. That is, each pixel of the OH images meeting the simultaneous gradient and curvature conditions was identified as flame surface. The resultant contours could vary with the same resolution as the OH-PLIF images, and thus exhibited discrete pixelization that affected the curvature calculation. This pixelization was removed by smoothing the contours with a five pixel moving average filter. The smallest scale corrugations that could be identified therefore were approximately of 5 pixels or 1.57 mm. This scale is on the order of the reaction layer thickness. Hence, the resolution of the flame curvature calculations was sufficient to describe the flame topography. The robustness of the routine was checked by varying the threshold on the OH gradient. The curvature statistics were compiled from the

axial region between $y = 0$ mm and 20 mm, which was the region with the greatest signal-to-noise ratio. In this region, varying the threshold level over a reasonable range produced only minor variations in the individual flame contours. The qualitative results and statistical trends were independent of the threshold employed.

4 Results and Discussions

In general both E5 and E6 flames burned stably without any thermoacoustic oscillations under all operation conditions investigated. Previous flow field investigations at atmospheric pressure [16], but comparable flow conditions, have shown that the flames are stabilized by a strong inner recirculation zone (IRZ) and a less pronounced outer recirculation zone (ORZ). The IRZ extends from the bluffbody to nearly the top of the combustion chamber, while the ORZ is squeezed between the combustor walls and the combustion zone. Two reaction zones, the first between the fuel and the air inflows and the second between the fuel inflow and the recirculating burned gases, were observed at the nozzle exit for all investigated cases. The strength of these reaction zones however depended on the operating condition as will be seen later. The images shown in the following section are cropped from the full field-of-view (approximately 177×145 pixels (height \times width)) for clarity. The flame structure and the regions of high temperature were identified using the OH-PLIF images, while the size, shape and location of the heat release zone was visualized using the OH* chemiluminescence images.

4.1 Influence of Varying Pressure on the Flame Structure

To begin, the effects of pressure on the structure of the E5 flames will be discussed. Figure 3 shows instantaneous OH-PLIF images along with the ensemble average and RMS fluctua-

tions of OH-PLIF images for the E5 flame at an equivalence ratio $\phi = 0.5$, pressures $p = 5, 10, 15$ and 20 bar, and $P_{th} = 15$ kW/bar. Zoomed in views of the region at a radius between $r = 10$ mm and 25 mm and axial distance between $y = 5$ mm and 20 mm are shown as insets. The ensemble average and RMS images were created from 200 single-shot images. In the figures, the laser sheet traversed from left to right and only the region on the left half of the burner axis is shown. Due to absorption of the laser radiation by OH radicals, the right half of the original images had lower LIF intensities than the left half. Therefore only the regions on the left half of the burner axis are considered for the interpretation of the results in this paper. Also, the laser sheet starts at a distance of approximately 2 mm downstream from the nozzle exit. At higher chamber pressures, the signal-to-noise ratio of the OH-PLIF images was drastically reduced due to molecular line broadening of OH transitions. For example, the average signal-to-noise ratio (S/N) decreased from approximately 10 at 5 bar to 2.4 at 20 bar for the images shown in Fig. 3. If the maximum signal of the time averaged image is set to 1 at 5 bar, the levels are 0.38, 0.21, and 0.1 at 10, 15 and 20 bar, respectively. This obviously hinders the direct comparison of OH-LIF intensities corresponding to different operational pressures. However, to facilitate the comparison of flame spatial characteristics, shape, size at different operating conditions, the intensity of all OH-PLIF images shown in this paper are scaled from zero to the maximum value .

The two distinct flame zones near to the nozzle exit are clearly visible in the averaged images. These two flame zones merge at few millimeters downstream of the nozzle exit. The appearance of grainy structures at downstream locations at high pressures are due to the very low S/N in these regions. For comparison, at $p = 20$ bar, the average S/N ratio at the flame front was approximately 3.9 whereas at the IRZ it was about 1.4. Previous flowfield measurements in this burner under similar flow conditions has shown intense mixing between the fresh gases and the recirculating burned gases at the shear layers [18]. Therefore,

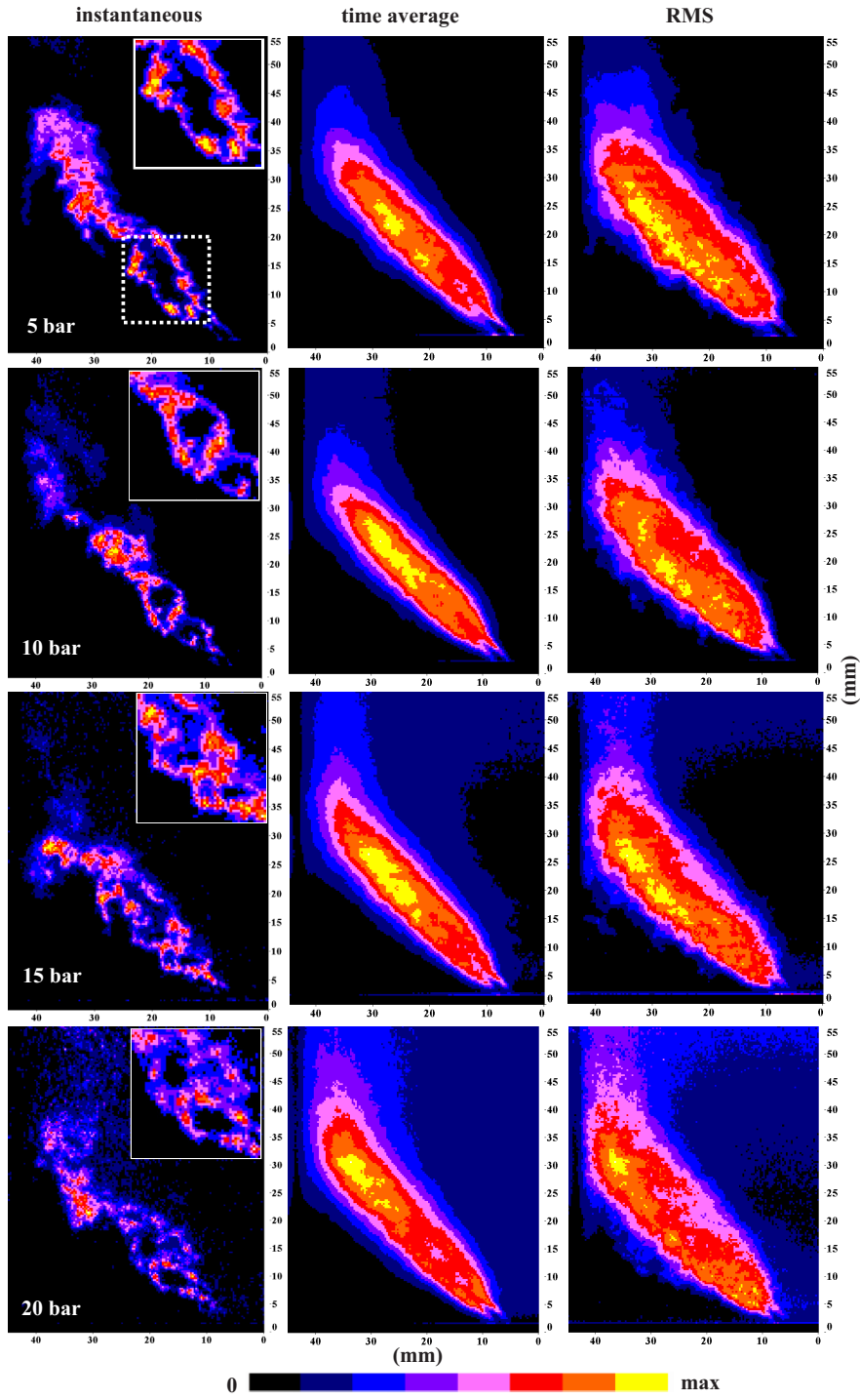


Fig. 3 The OH single shots, time average and RMS fluctuations for the E5 flame ($P_{th} = 15 \text{ kW/bar}$) at $p = 5, 10, 15$ and 20 bar . Inset: Zoomed in views of the region marked by dotted lines.

a fair amount of premixing before ignition of the flame is expected near the nozzle exit. The reaction zones are expected to be established at near stoichiometric mixtures close to the exit, but more on the fuel rich side of stoichiometric mixture fraction. However, further downstream, the mixture becomes more and more fuel lean as the equivalence ratio approaches $\phi_{global} = 0.5$. While the size of the large scale structures is relatively fixed by the geometry, the evolution of small scale structures downstream could be influenced by a variety of mechanisms. The flowfield at downstream locations will be influenced by the gradual development of the shear layer instability, where a portion of the net kinetic energy is transferred to the small scale structures. In addition, the inner flame front resides in a region of higher shear rate than the outer flame front, whereas the temperature gradient at the outer flame front is higher than at the inner flame front. These gradients enhance the turbulence intensities at the inner and outer flame fronts, respectively. All these effects will aid in the formation of highly corrugated structures with increasing distance from the nozzle exit. It can also be seen that the distributions have become more noisy with increasing pressure. This is at least partly due to the lower S/N level at high p as discussed before. However, it can also be observed that the structures become smaller and speckled (see insets). This is due to an increase in Reynolds number (Re) with increasing pressure ($\rho \propto p$). Interestingly, the RMS fluctuations of the LIF intensity at downstream locations are more intense at the outer reaction zone than at the inner reaction zone. The reason for the higher stability of the inner flame can be manifold. Firstly, the inner flame is better stabilized than the outer flame due to the high temperature of the recirculating burned gases in the IRZ. Secondly, the reactivity of the outer flame is lower than that of the inner flame due to the dependence of reaction rate on mixture temperature. This implies that the outer flame will locally extinguish more readily than the inner flame.

At lower pressures, for example at $p = 5$ bar, the formation of OH at superequilibrium concentrations and its convective transport cannot be neglected. OH is produced at superequilibrium concentrations in the reaction zone before it decays to chemical equilibrium downstream [2, 22, 23]. The three body radical decay reactions, which are pressure sensitive, proceed in a timescale of milliseconds to microseconds for atmospheric and high pressure flames, respectively. For example, at $p = 10$ bar the decay time is around $10 \mu s$, by which time the fluid elements would have convected a distance of almost 1 mm. This means that the broad region of high OH intensities seen in the single shot image at 5 and 10 bar may be an outcome of the transport of the superequilibrium OH concentration. However, at high pressures the effect is not significant. The ensemble averaged images at different pressures also show that the region of high OH intensity remains more or less unaffected by pressure with respect to size and location.

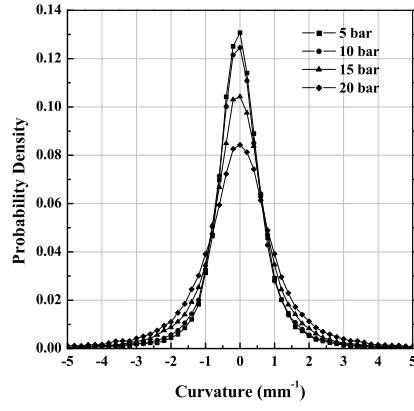
The interpretation of the OH intensity versus pressure is not straightforward. The is because, OH concentration has a complex relationship with burning velocity, mixture composition, Lewis number and strain rate. The H_2 rich mixtures in general have maximum burning velocity in the fuel rich side of the stoichiometric equivalence ratio, ϕ_{stoi} while the OH has maximum concentrations at $\phi = \phi_{stoi}$. The maximum burning velocity is also pressure dependent with drastic reduction at high pressures [12]. At downstream locations, where the ϕ shifts towards ϕ_{global} , the reaction zone also is expected to shift from the fuel rich side towards the fuel lean side, further complicating the interpretation of OH-LIF distribution. The impact of non-unity Lewis number, especially at lower pressures, on the flame temperature and corresponding OH concentration is another factor that complicates the interpretation of the result. At low pressures, the smaller size of hydrogen enhances the diffusion of H and H_2 into the reaction zone thereby increasing the reactivity. But as pressure increases, the simultaneous decrease in diffusivity hinders the preferential diffusion of hydrogen thereby

influencing the OH concentration. In addition, the local strain rates also play an important role. For example, a H_2 /air mixture has a non-monotonic relationship between pressure and extinction strain rates (indicative of the reaction intensity) [24]. All these factors point that the interpretation of the OH-PLIF signals with pressure require detailed analysis of the individual influencing parameters and their interactions.

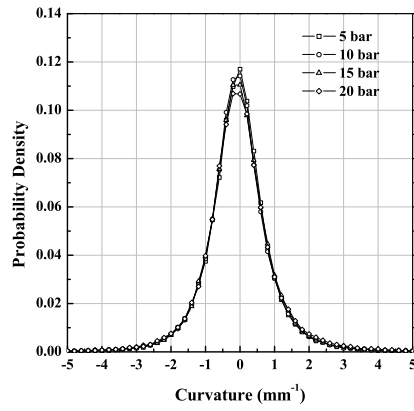
It is clear from the single shot OH-PLIF images that there is a significant change in the flame front curvature with changing pressure. In order to gain better understanding of the mechanisms behind the generation of the flame front wrinkling, quantification of the pressure induced curvature is necessary. Figures 4(a) and 4(b) show the probability density function (pdf) of the flame curvature at the different pressures for the inner and outer flames, respectively. In Fig. 5, the variation of the mean curvature magnitude with pressure is summarized. Only the flame zone within the first 20 mm in the axial and radial directions are used for the estimation of the pdfs as the OH-LIF S/N ratio is considerably better in this region at higher pressures. The pdf distributions are nearly Gaussian with equal probabilities of positive and negative curvature for both the inner and outer flames. At low pressures, when the flame is thicker, the curvature provides a stabilizing effect to small scale perturbations in the flow. In the case of constant strain rates, the flame thickness evolves like the inverse square root of pressure [25]. Therefore the flame thickness decreases as the pressure is increased. The different responses of the curvature pdfs for the inner and outer flames with increasing pressure is consequentially surprising. The inner and outer flames respond differently to pressure as can be seen from the pdfs. While there is hardly any change in the pdf for the outer flame, the inner flame distribution broadens. This might indicate an increase in small scale turbulence intensity with pressure in the inner flame, whereas the outer flame curvature remains more or less constant in the investigated pressure range. This also is exhibited in Fig. 5, where the increase in mean curvature magnitude, which represents

the degree of flame wrinkling with pressure, is shown. Also recognizable is the fact that at $p = 5$ bar the outer flame is more wrinkled than the inner flame. While the outer flame curvature remains more or less unaffected by the pressure increase, the inner flame wrinkling increases strongly with pressure and becomes more wrinkled than the outer flame between 10 and 15 bar.

In order to understand the fundamental mechanism behind the wrinkling process, it is necessary to have a closer look at the pressure impact on turbulence. The main pressure influence on turbulence stems from the strong decrease in kinematic viscosity ν with increasing pressure, $\nu \sim p^{-1}$. The local Reynolds number $Re = u' l_x / \nu$, where u' and l_x are the velocity fluctuations and the integral length scale, respectively, increases as a result, leading to a corresponding decrease in the size of the small turbulent scales (more small scale wrinkling) with pressure. With increasing Re and decreasing ν , even the smaller vortices may be able to withstand the viscous dissipation in the flame, resulting in an increase in the turbulence intensities. Since the fuel and air mass flow rates increase with increasing pressure for a constant inflow velocity, the fuel consumption rate is increased by an increase in the flame surface area and also by an increase in the reaction rate. However, the reason for the dissimilar variation of the curvature magnitude with pressure for the inner and outer flame is not clear at present. Due to the multiple simultaneous phenomena affecting the flame in this configuration, the specific cause or causes of the flame wrinkling behavior could not be identified. However, the investigated flame can be considered as similar to a stratified flame with a lean outer flame front and a rich inner flame front. So, future work should address this issue by conducting simplified and controlled, multi-stream experiments. In particular, the behavior of high pressure stratified flames in transverse velocity and temperature gradients should be studied, such as those previously conducted for atmospheric pressure flames [26].



(a)



(b)

Fig. 4 Variation of flame curvature distribution with pressure for the inner flame (a) and outer flame (b) of E5 deduced from the OH-PLIF images.

In case of axisymmetric flames, the time averaged OH* images can be deconvoluted to yield spatially resolved planar information. The deconvoluted chemiluminescence image of the E5 flames obtained from the time averaged OH* (electronically excited) images are shown in Fig.6 at different pressures and $P_{th} = 15 \text{ kW/bar}$. As with the OH-PLIF images,

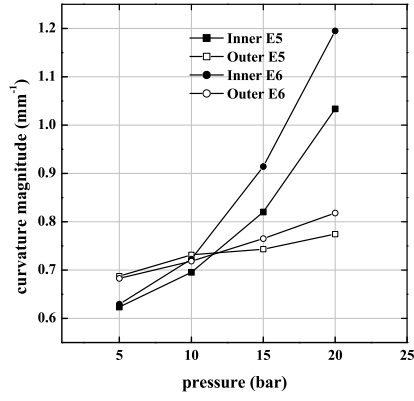


Fig. 5 Variation of mean curvature magnitude of the inner and outer flame front with pressure for the E5 flame and E6 with $P_{th} = 15\text{kW/bar}$.

only the region corresponding to the left half of the burner is shown and all the images are scaled to the same intensity range for ease of comparison. The heat release zone extends to a maximum height of 20 mm, the variation of the heat release zone dimensions with pressure is marginal, and the shapes are similar. The flame height decreases a little as the pressure is increased from 5 - 10 bar, after which it grows back to the original dimension for a pressure increase from 10 - 20 bar. Similar to the OH-PLIF images, the inner and outer heat release zones are clearly identifiable close to the nozzle exit before they merge downstream. It is important to note that, though the total thermal power increased with increasing pressure, the total OH* intensity did not change significantly. The average S/N ratio in the raw images varied only slightly, from 15 at 10 bar to about 18 at 20 bar. One probable explanation could be the effect of quenching of OH* with increasing pressure. This clearly shows the limitations of OH* chemiluminescence as a measure for the heat release rates for all fuels, as has been reported in previous literatures [27].

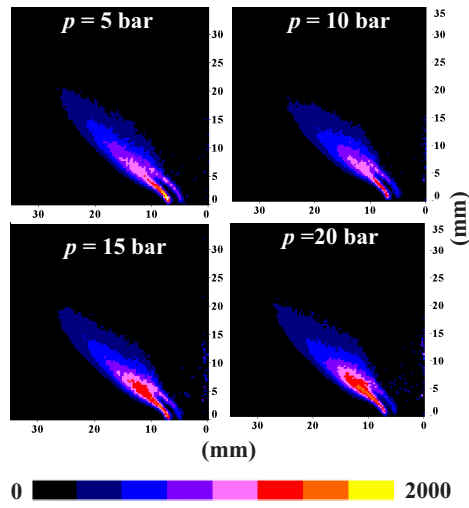


Fig. 6 Abel deconvoluted OH* chemiluminescence images at pressure $p = 5, 10, 15$ and 20 bar for the E5 flame and $P_{th} = 15$ kW/bar.

4.2 Variations in Mixture Composition

In addition to the pressure, the specific syngas composition greatly affects the combustion properties. The instantaneous, ensemble averaged, and RMS fluctuations of the OH-PLIF image for the E6 flames ($P_{th} = 15$ kW/bar) at $p = 5, 10, 15$ and 20 bar are shown in Fig. 7. The length of the E6 flames are greater than those of the E5 flames at all pressures, with a broader OH-PLIF distribution seen in the averaged images. Also, the region with high OH-LIF intensities is shifted further downstream compared to the E5 flames and the shift increases with increasing pressure. This seems to indicate that for the same pressure, the E6 flames are less reactive than the E5 flames and the reaction rate decreases with increasing pressure. Conversely, the region of maximum RMS fluctuations is more concentrated compared to the E5 flames. One of the factors that might be influencing the flame height is the decrease in reactivity of E6 due to the presence of CH_4 in the mixture. Previous investigations by other research groups have shown a substantial reduction in laminar flame speed, s_L

(which is a measure of the reactivity of the mixture) for various hydrocarbon substituted H_2 -air and syngas mixtures [28,29]. For example, experimental and numerical investigations by Law et al. have shown that in case of hydrogen-air mixtures at a global equivalence ratio of 0.6, s_L decreased from approximately 800 mm/s to about 400 mm/s for a 40% volumetric substitution of H_2 by CH_4 [28]. This means that the combustion is faster for the E5 flames when compared to the E6 flames, resulting in the observed difference in the flame length. In the H_2 dominated regime (10 - 100 % H_2 in CO) CO was found to play only a minimal role in the ignition behaviour with the dominant kinetics involving only H_2 chemistry [4, 5, 12]. So, the increase in flame height with pressure highlights the decrease in laminar burning velocity of the E6 flames with increasing pressure for hydrocarbon substituted H_2 -air, as reported in [28].

Figures 8(a) and 8(b) show the distribution of flame curvature and its dependence on pressure for the E6 flame at the inner and outer flame front, respectively. Similar to the results for E5 the pdfs for both the inner and outer flame front show symmetrical Gaussian like distribution. Also there is a significant intensification of the convolution in the inner flame with pressure compared to the outer flame. The increase in curvature magnitude with pressure is also mirrored in the mean curvature magnitude versus pressure plot in Fig.5. The relatively higher mean curvature magnitude of E6 with respect to E5 at all pressures indicates that the E6 is less stable than E5. The flame thickness increases with hydrocarbon substitution in most cases, which in turn can improve the stability of the mixture. But the decreased flame stability of E6 with respect to E5, as seen in Fig.5, implies that the stabilizing effect of increase in flame thickness is not so effectual and is outweighed by the destabilizing effect produced probably by the subsequent decrease in the laminar flame speed.

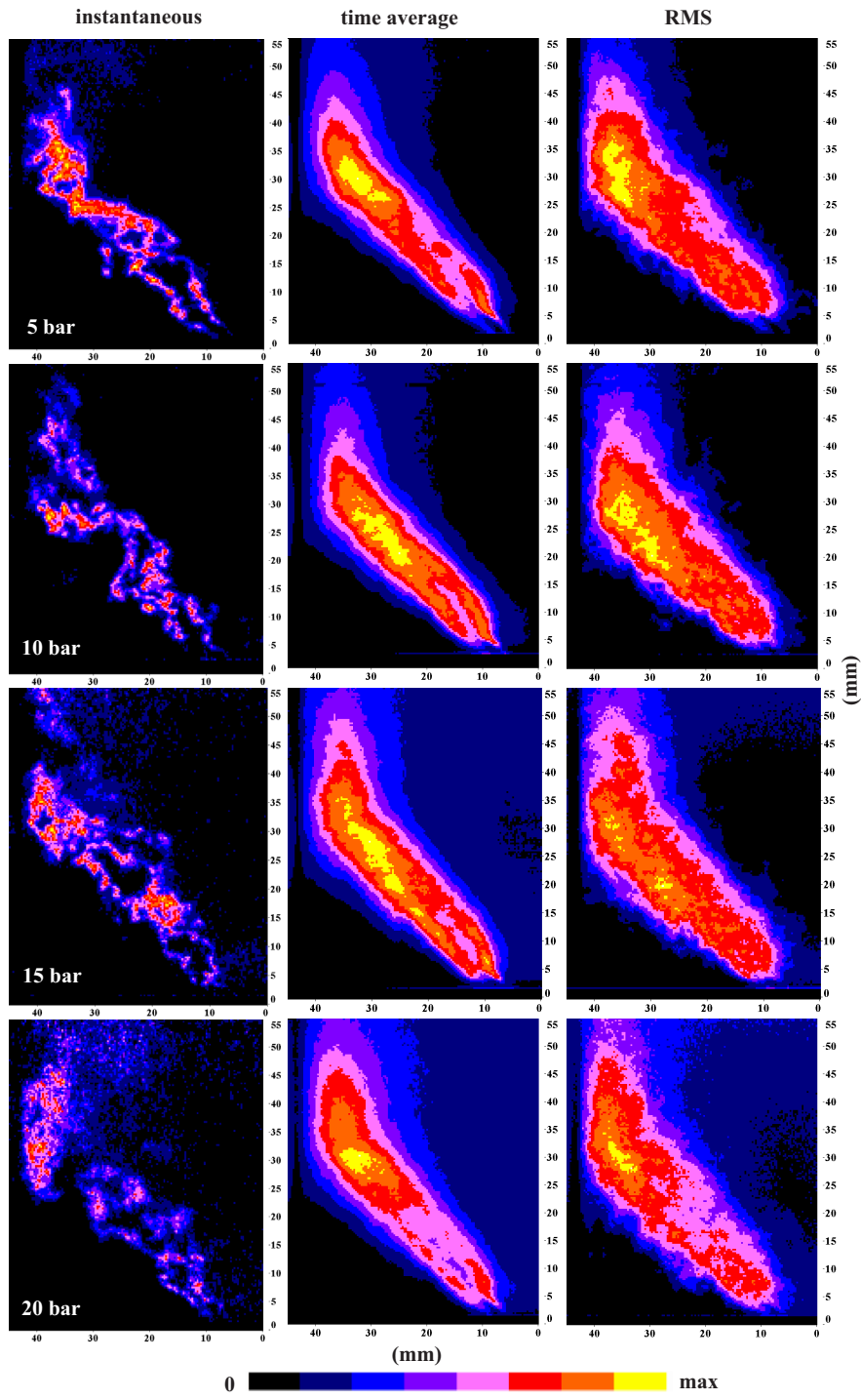
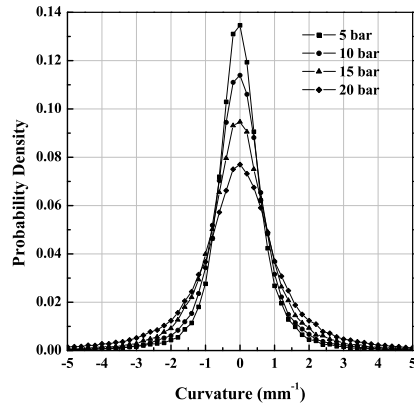
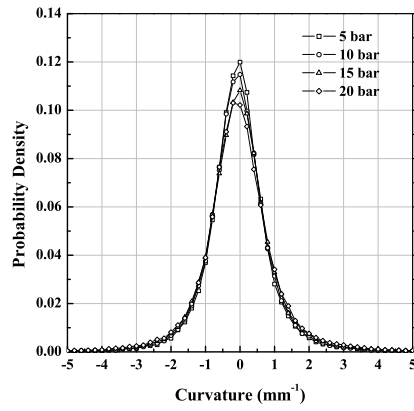


Fig. 7 The OH single shot, time average and RMS fluctuations for the E6 flame ($P_h = 15 \text{ kW/bar}$) at $p = 5, 10, 15$ and 20 bar .



(a)



(b)

Fig. 8 Variation of flame curvature distribution with pressure for the inner flame (a) and outer flame (b) of E6 deduced from the OH-PLIF images.

The deconvoluted OH* chemiluminescence image deduced from the time averaged OH* images for the E6 flames are shown in Fig.9. There is an appreciable increase in the size of the heat release zone with increasing pressure. Analogous to E5, the OH* intensity in the inner flame remains more or less constant from 5 to 20 bar, whereas the reaction rate in the

outer flame region shows a steady increase for the E6 flame. This is in contrast to the effect of pressure on the heat release rate of E5 flame.

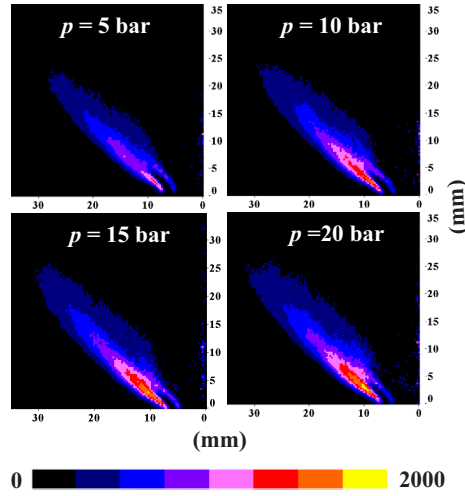


Fig. 9 Abel deconvoluted OH* chemiluminescence images at pressure $p = 5, 10, 15$ and 20 bar for the E6 flame and $P_{th} = 15$ kW/bar.

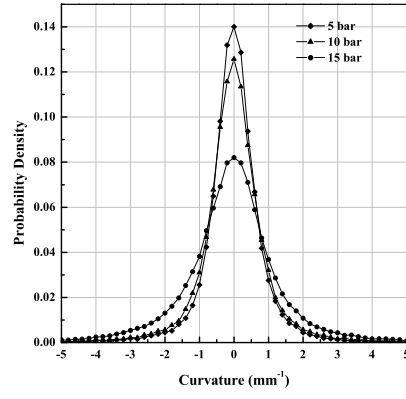
4.3 Influence of the Variations in Thermal Power on Flame Structure

Finally, the variation of flame curvature distribution with pressure at the inner and outer flame for the mixture E5 at $P_{th} = 25$ kW/bar is shown in Fig. 10(a) and Fig. 10(b). Also shown in Fig. 11 is the variation in average flame curvature magnitude with pressure at the same thermal power. The curvatures were deduced from the OH-PLIF images (not shown) as before. The outer flame curvature distribution is slightly skewed towards negative curvature values. The variation of flame curvature magnitude with pressure shows a completely different picture for the outer flame front compared to what was seen for E5 at $P_{th} = 15$ kW in the previous section. Up to a pressure of 10 bar, the curvature magnitude of both inner and outer flames is almost identical to the 15 kW case. However, the pdfs broaden as the pressure

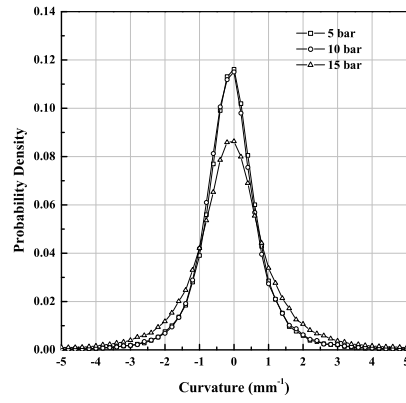
is raised to 15 bar, indicating an increase of the flame curvature magnitude on both fronts. From Fig. 11, it can be seen the intensification is only slightly higher in the inner front than in the outer front. An increase in P_{th} will result in qualitatively different scenarios in the shear layer of inner and outer flame front: (i) it increases the mixing rate between the fuel and the air in the outer region, and between the fuel and the burned gases in the inner region (ii) it induces a higher strain rate, and thereby a lower residence time, at the mixing layers. By considering the combined effect of pressure and strain rate on the flame thickness, it was seen that the thickness is inversely proportional to both strain rate and pressure [25]. This double impact will create instability in both inner and outer flame making them vulnerable to the wrinkling process more readily than E5 at $P_{th} = 15$ kW.

5 Conclusions

Optical and laser diagnostic methods were applied in an optically accessible swirl flame burner operated with syngas mixtures and preheated air at elevated pressures. OH-PLIF and OH* chemiluminescence measurements were performed to investigate the influence of pressure on the flame characteristics. Two syngas mixtures, designated E5 and E6, were investigated in the current studies, with E5 consisting of H₂, N₂ and CO and E6 with H₂, N₂, CO and CH₄. From previous velocity measurements at atmospheric conditions, it is known that the flowfield consisted of a strong inner recirculation zone, a weak outer recirculation zone, and a conical inflow of fresh air in between these two regions. The OH-PLIF images showed two flame fronts at the inner shear layer, the first one between the inner recirculation zone and the fuel inlet and the second one between the fuel inlet and the air nozzle. E6 flames differed from the E5 flames in OH-PLIF distribution by having a greater flame height, broader OH distribution and a shift in maximum OH-LIF intensities further downstream



(a)



(b)

Fig. 10 Variation of flame curvature distribution with pressure for the inner flame (a) and outer flame (b) of E5 at $P_{th} = 25\text{kW/bar}$ deduced from the OH-PLIF images.

from the nozzle exit. In particular, the increase in flame height implies that the hydrocarbon substituted E6 flames are less reactive than the E5 flames.

To investigate the mechanisms behind the flame front wrinkling with pressure, quantification of the pressure induced curvature was performed on the OH-PLIF images of both E5

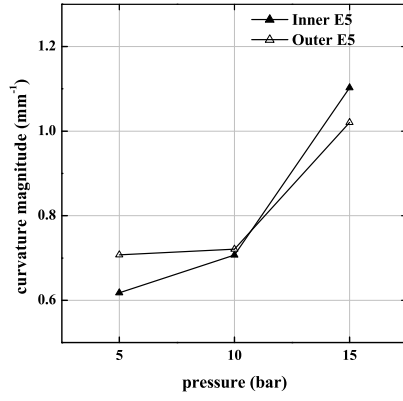


Fig. 11 Variation of mean curvature magnitude of the inner and outer flame front with pressure for the E5 flame with $P_{th} = 25\text{kW/bar}$.

and E6 flames. From the probability density function of the flame curvatures, it was seen that the inner flame front wrinkled more intensely than the outer flame front with increasing pressure at lower thermal loads. The mean curvature magnitude of E6 was greater than E5 at both the inner and outer flame fronts. However, the corrugation of both the inner and outer E5 flames increased greatly at higher thermal loads. Due to the multiple simultaneous phenomena affecting the flame, it was not possible to identify the specific cause or causes of the flame wrinkling behavior.

The two heat release zones were also clearly identifiable in the deconvoluted OH* chemiluminescence images. But the heat release zone characteristics varied differently with pressure for the E5 and E6 flames. Moreover, the OH* intensity did not change significantly with the increasing total thermal power for both cases, as one would expect. This shows that the adequacy of OH* as a marker for the heat release rate is questionable for the conditions investigated here.

6 Acknowledgements

The work presented here has been carried out in the framework of the national COORETEC initiative as part of the project VESKO ("Verbrennung von Synthesegas aus Kohle in Gasturbinen", 0327700Z), which is funded by the German Federal Ministry of Economics and Technology. The authors take the responsibility for the content of the paper. The authors would also like to acknowledge the support of U. Prestel and K.H. Ferst.

References

1. P. Røkke, J. Hustad, *International Journal of Thermodynamic* **8**(4), 167 (2005)
2. M. Drake, *Proceedings of the Combustion Institute* **21**, 1579 (1986)
3. C. Vagelopoulos, F. Egolfopoulos, *Proceedings of the Combustion Institute* **25**, 1317 (1994)
4. J. Trujillo, T. Kreutz, C. Law, *Combustion Science and Technology* **127**(1), 1 (1997)
5. C. Fotache, Y. Tan, C. Sung, C. Law, *Combustion and Flame* **120**, 417 (2000)
6. G. Smith, D. Golden, M. Frenklach, N. Moriarty, B. Eiteneer, M. Goldenberg, C. Bowman, R. Hanson, S. Song, W. Jr., V. Lissianski, Z. Qin. http://www.me.berkeley.edu/gri_mech
7. S. Davis, A. Joshi, H. Wang, F. Egolfopoulos, *Proceedings of the Combustion Institute* **30**, 1283 (2004)
8. M. Drake, X. Qin, Y. Ju, F. Dryer, in *Proceedings of the 5th US Combustion Meeting* (San Diego, United States, 2007), p. A16
9. H. Sun, S. Yang, G. Jomaas, C. Law, *Proceedings of the Combustion Institute* **31**, 439 (2007)
10. J. Natarajan, Y. Kochar, T. Lieuwen, J. Seitzman, *Proceedings of the Combustion Institute* **32**, 1261 (2009)
11. J. Natarajan, T. Lieuwen, J. Seitzman, *Combustion and Flame* **151**, 104 (2007)
12. C.J. Sung, C. Law, *Combustion Science and Technology* **180**(6), 1097 (2008)
13. A. Eckbreth, *Laser diagnostic for combustion temperature and species*, 2nd edn. (Gordon and Breach, Netherlands, 1996)
14. K. Kohse-Höinghaus, J. Jeffries(Eds.), *Applied Combustion Diagnostics* (Taylor and Francis, New York, 2006)

-
15. M.D. Domenico, P. Kutne, C. Naumann, J. Herzler, R. Sadanandan, M. Stöhr, B. Noll, M. Aigner, in *Proceedings of the ASME Turbo Expo 2009* (Orlando, United States, 2009), GT2009-59308
 16. P. Kutne, I. Boxx, M. Stöhr, W. Meier, in *Proceedings of the European Combustion Meeting 2007* (Chania, Greece, 2007), pp. 23–4
 17. S. Pater, J. Kok, T.V. der Meer, in *Proceedings of the ASME Turbo Expo 2006* (Barcelona, Spain, 2006), GT2006-90910
 18. M. Tsurikov, W. Meier, K.P. Geigle, in *Proceedings of the ASME Turbo Expo 2006* (Barcelona, Spain, 2006), GT2006-90344
 19. V. Nori, Modelling and analysis of chemiluminescence sensing for syngas, methane and jet-a combustion. Ph.D. thesis, Georgia Institute of Technology (2008)
 20. J. Donbar, J. Driscoll, C. Carter, *Combustion and Flame* **125**, 1239 (2001)
 21. R. Sadanandan, M. Stöhr, W. Meier, *Applied Physics B* **90**, 609 (2008)
 22. M. Drake, R. Pitz, M. Lapp, C. Fenimore, R. Lucht, D. Sweeney, N. Laurendeau, *Proceedings of the Combustion Institute* **20**, 327 (1984)
 23. R. Barlow, R. Dibble, J.Y. Chen, R. Lucht, *Combustion and Flame* **82**, 235 (1990)
 24. C.K. Law, *Combustion Science and Technology* **178**(1), 335 (2006)
 25. L. Pons, N. Darabiha, S. Candel, *Combustion and Flame* **152**(1), 218 (2008)
 26. M. Sweeney, S. Hochgreb, M. Dunn, R. Barlow, *Proceedings of the Combustion Institute* **33**, 1419 (2011)
 27. H. Najm, P. Paul, C. Mueller, P. Wyckoff, *Combustion and Flame* **113**, 312 (1998)
 28. C. Law, O.C.Kwon, *International Journal of Hydrogen Energy* **29**, 867 (2004)
 29. V. Kishore, M. Ravi, A. Ray, *International Journal of Reacting Systems* **310740** (2008)